OPEN ACCESS



Effective Resistivity in Relativistic Collisionless Reconnection

S. Selvi 1, O. Porth 1, B. Ripperda 2,3,4,8, F. Bacchini 5,6, L. Sironi 7, and R. Keppens 1, Anton Pannekoek Institute, Science Park 904, 1098 XH, Amsterdam, The Netherlands; s.c.selvi@uva.nl 2, School of Natural Sciences, Institute for Advanced Study, 1 Einstein Drive, Princeton, NJ 08540, USA 3, Princeton University, Department of Astrophysical Sciences, 4 Ivy Lane, Princeton, NJ 08544, USA 4, Flatiron Institute, Center for Computational Astrophysics, 162 Fifth Avenue, New York, NY 10010, USA 5, Centre for mathematical Plasma Astrophysics, Department of Mathematics, KU Leuven, Celestijnenlaan 200B, B-3001 Leuven, Belgium 6, Royal Belgian Institute for Space Aeronomy, Solar-Terrestrial Centre of Excellence, Ringlaan 3, 1180 Uccle, Belgium 7, Columbia University, Department of Astronomy, 550 West 120th, New York, NY 10027, USA Received 2022 September 1; revised 2023 April 20; accepted 2023 April 25; published 2023 June 22

Abstract

Magnetic reconnection can power spectacular high-energy astrophysical phenomena by producing nonthermal energy distributions in highly magnetized regions around compact objects. By means of two-dimensional fully kinetic particle-in-cell (PIC) simulations, we investigate relativistic collisionless plasmoid-mediated reconnection in magnetically dominated pair plasmas with and without a guide field. In X-points, where diverging flows result in a nondiagonal thermal pressure tensor, a finite residence time for particles gives rise to a localized collisionless effective resistivity. Here, for the first time for relativistic reconnection in a fully developed plasmoid chain, we identify the mechanisms driving the nonideal electric field using a full Ohm law by means of a statistical analysis based on our PIC simulations. We show that the nonideal electric field is predominantly driven by gradients of nongyrotropic thermal pressures. We propose a kinetic physics motivated nonuniform effective resistivity model that is negligible on global scales and becomes significant only locally in X-points. It captures the properties of collisionless reconnection with the aim of mimicking its essentials in nonideal magnetohydrodynamic descriptions. This effective resistivity model provides a viable opportunity to design physically grounded global models for reconnection-powered high-energy emission.

Unified Astronomy Thesaurus concepts: High energy astrophysics (739); Plasma astrophysics (1261); Compact objects (288); Magnetic fields (994); Relativity (1393); Magnetohydrodynamics (1964)

1. Introduction

In magnetospheres, jets, and accretion disk coronae of black holes and neutron stars, relativistic magnetic reconnection is widely conjectured as the mechanism powering many spectacular high-energy phenomena such as flares from black hole magnetospheres (Nathanail et al. 2020; Ripperda et al. 2020; Chashkina et al. 2021; Nathanail et al. 2022; Ripperda et al. 2022), black hole accretion disk coronae (Sironi & Beloborodov 2020; Sridhar et al. 2021, 2022), neutron star binary merger precursors (Most & Philippov 2020), neutron star-black hole postmerger emission (Lyutikov & McKinney 2011; Bransgrove et al. 2021), fast radio bursts (Lyubarsky 2020; Lyutikov & Popov 2020; Mahlmann et al. 2022; Most & Philippov 2022), coherent radio and gamma-ray pulsar magnetospheric emission (Lyubarsky 2018; Philippov & Spitkovsky 2018; Philippov et al. 2019; Hu & Beloborodov 2021), giant magnetar flares (Parfrey et al. 2012), gamma-ray flares from pulsar wind nebulae (Cerutti et al. 2012; Lyubarsky 2012), and flares from blazar jets (Giannios 2013; Petropoulou et al. 2016).

The highly magnetized predominantly pair plasma in these environments acts as a reservoir of magnetic energy that can be converted by magnetic reconnection into kinetic and thermal energy and radiation, powering the high-energy emission. The majority of these systems is collisionless,

Original content from this work may be used under the terms of the Creative Commons Attribution 4.0 licence. Any further distribution of this work must maintain attribution to the author(s) and the title of the work, journal citation and DOI.

meaning that the mean free path of electrons is (much) larger than the system size, such that particles can accelerate to high energies and form nonthermal energy distributions in reconnecting current sheets. Reconnection occurring in the collisionless regime requires a kinetic description. However, the typical scale separation between plasma scales and the global scales of astrophysical systems is extremely large, such that kinetic descriptions, e.g., widely employed particlein-cell (PIC) methods, are unaffordable at realistic scales. Fluid-type descriptions such as magnetohydrodynamics (MHD) are typically more suitable for modeling global systems, but are by construction collisional, and are therefore unable to capture collisionless reconnection. The desire to accurately model reconnection-powered phenomena and their high-energy emission in global systems asks for the incorporation of the properties of collisionless reconnection in an MHD description. In the standard relativistic collisional one-fluid description, an explicit finite resistivity can serve as a macroscopic proxy (Del Zanna et al. 2016; Ripperda et al. 2019, 2019) for breaking Alfvén's frozen-in condition, thereby enabling reconnection. A physically motivated model for the resistivity in the relativistic reconnection regime is lacking so far, where the inability of MHD to fully capture the properties of collisionless reconnection is exposed by, for example, the discrepancy of a factor ~10 between collisional and collisionless reconnection rates in the plasmoid regime (Uzdensky et al. 2010; Comisso & Bhattacharjee 2016). This difference may affect the typical timescales of reconnection-powered high-energy emission (Bransgrove et al. 2021).

⁸ NASA Hubble Fellowship Program, Einstein Fellow.

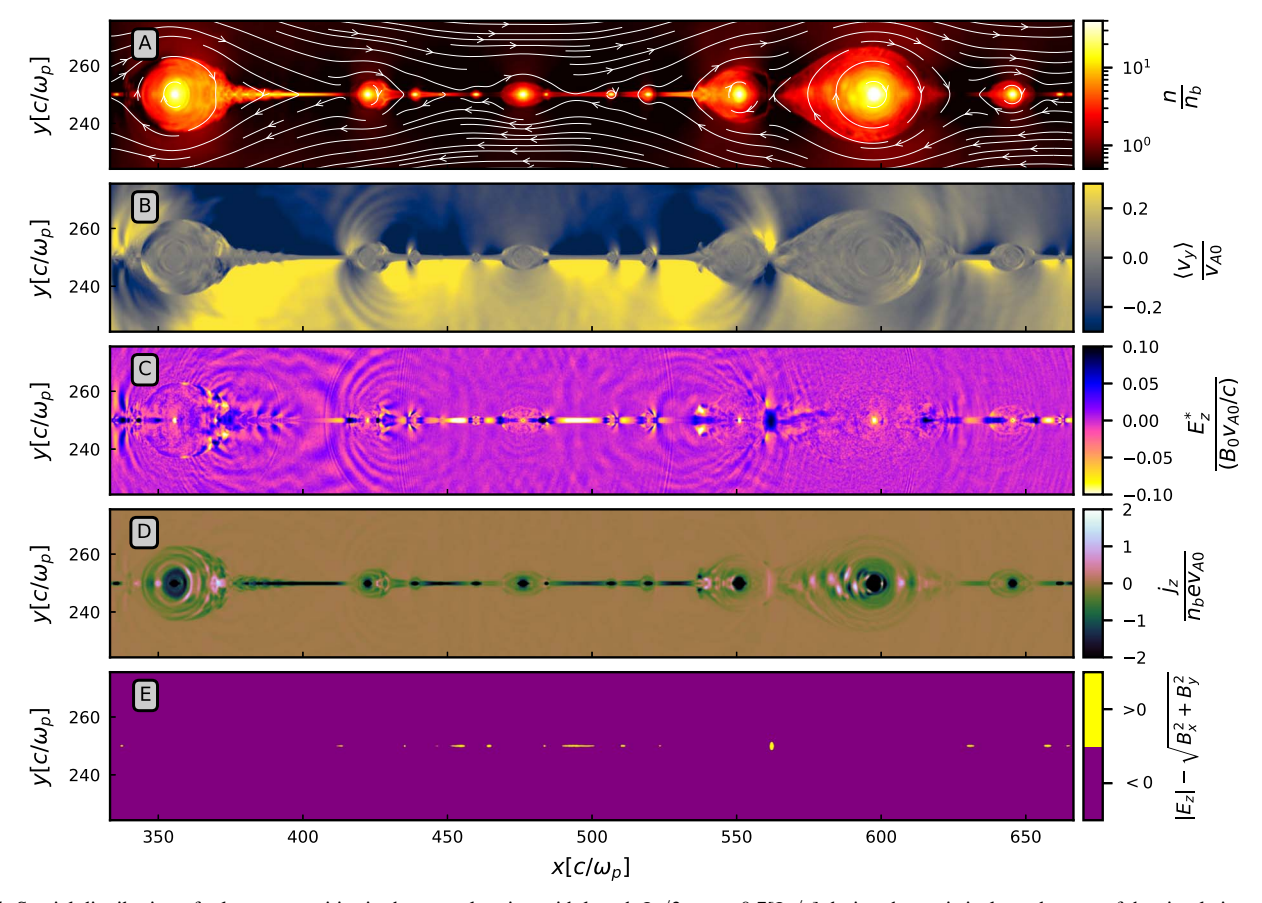


Figure 1. Spatial distribution of relevant quantities in the central region with length $L_x/3$ at $t=0.7[L_x/c]$ during the statistical steady state of the simulation without a guide field. From the top to the bottom panel, panel (A) shows the particle number density n in units of the initial upstream number density n_b , showing a hierarchical plasmoid chain as overdense regions. Panel (B) shows the mean particle inflow velocity $\langle v_y \rangle$ in units of the initial upstream Alfvén velocity v_{A0} , showing plasma (continuously) being advected into the central region by the reconnection process. Panel (C) shows the out-of-plane nonideal electric field E_z^* in units of B_0v_{A0}/c , showing regions where accelerating reconnection electric fields are created in X-points and magnetic energy is dissipated. Panel (D) shows the out-of-plane current density j_z in units of n_bev_{A0} . Panel (E) shows reconnection regions (in yellow) defined as $|E_z| > (B_x^2 + B_y^2)^{1/2}$, identifying the nonideal regions of interest in X-points where reconnection occurs.

Our goal is to propose a kinetic physics motivated model for the resistivity that will pave the way for the modeling of global systems while taking the self-consistent properties of collisionless reconnection into account. To be able to propose such an effective resistivity model, in this work, we investigate relativistic collisionless pair plasma reconnection by means of two-dimensional (2D) fully kinetic PIC simulations. Here, for a fully developed plasmoid chain, we identify the reconnection mechanisms providing the nonideal electric field using a full Ohm law. In contrast to previous studies, we analyze selfconsistently formed secondary X-points in a fully developed plasmoid chain instead of primary X-points dominated by initial conditions. We present a statistical analysis of all (secondary) X-points in the full plasmoid chain during its entire statistical steady state. The effective resistivity model proposed in this work provides a viable opportunity to mimic the essential properties of relativistic collisionless reconnection in a pair plasma in nonideal MHD simulations and to design physically grounded global models for reconnection-powered high-energy emission from magnetized (near-)collisionless systems.

2. Numerical Methods and Setup

Relativistic reconnection is studied in a 2D doubly periodic double current sheet system modeling an idealized magnetic

reconnection region. Herein, two regions of antiparallel magnetic field lines (in MHD setting, adopted from Keppens et al. 2013) are embedded in a pair plasma initialized in an equilibrium configuration. The magnetic field strength B_0 is parameterized by the plasma magnetization $\sigma = B_0^2/4\pi n_b mc^2$ of the cold background plasma, with n_b the total background plasma number density, and m the electron (and positron) mass. We focus on the relativistic regime with $\sigma = 10$ giving an initial upstream Alfvén speed $v_{A0} =$ $c\sqrt{\sigma/(1+\sigma)}\approx 0.95c$. For the kinetic simulations, we use the relativistic multispecies particle-in-cell (PIC) code Tristan-MP v2 (Hakobyan & Spitkovsky 2020). We performed three simulations, one without a guide field, and two with a guide field strength $0.25B_0$ and $0.5B_0$ up to a final time $t = 2[L_x/c]$. For guide field strengths $[0, 0.25]B_0$, we use a square 2D simulation domain with size $[L_x, L_y]$ = [1000, 1000] c/ω_p , with c/ω_p the skin depth and ω_p the plasma frequency, and initialize 160 particles per cell in total. For the simulation with a guide field strength $0.5B_0$, we use a domain size $[L_x, L_y] = [1000, 2000]c/\omega_p$ and initialize 40 particles per cell in total. In all simulations, we employ an initial current sheet width $\delta = 5c/\omega_{\rm p}$ and resolve the upstream skin depth with 10 grid cells. Throughout this work, all quantities are defined with respect to the simulation rest frame, and cgs units are used.

3. Results

Magnetic reconnection is initiated by an imposed small local magnetic field perturbation at the center of each current sheet, triggering a fast growing tearing mode. Reconnection fronts, propagating along the current sheet at approximately the Alfvén speed $v_{\rm A} \approx c$, sweep up the hot particles that provided the initial pressure support. Inside the large periodic simulation domain, we restrict our analysis to a smaller central region of interest, with length $L_x/3$, in which the properties of the resulting reconnecting current sheet in between the reconnection fronts are no longer subject to initialization after the two reconnection fronts have left this region. After this time, the plasma inflow velocity into the region and magnetic energy decay rate remain relatively constant, thereby establishing a statistical steady state in the analysis domain, which effectively has open boundaries within the larger simulation domain.

Figure 1 shows the spatial distribution of various quantities of interest, discussed next, in the central analysis region during this statistical steady state at $t = 0.7[L_x/c]$ for the simulation without a guide field. As the current sheet develops, a

mergers (e.g., Figure 1 at $x = 565[c/\omega_p]$), E_z^* and j_z are usually aligned. We ignore at any time $\sim 1-2$ regions on average in which they are anti-aligned. Without a guide field, we observe ~ 10 X-points in the analysis region simultaneously (Figure 1, panel (E)), while the guide field cases generate fewer X-points on average.

In order to capture the properties of collisionless reconnection, it is essential to describe the nonideal electric fields in the reconnection regions (i.e., the reconnection electric field). Therefore, in the following, we identify the mechanisms providing the reconnection electric field and determine their individual contributions using a full Ohm law for a pair plasma based on our PIC simulations.

3.1. Reconnection in a Single X-point

For a full Ohm law derived from first principles, by combining the momentum equations for positrons and electrons (Hesse & Zenitani 2007) and using that masses are the same and charges are opposite in a pair plasma, the out-of-plane *z*-component is

$$E_{z} = \underbrace{-\left(\frac{1}{c}\langle v_{t}\rangle \times \boldsymbol{B}\right)_{z}}_{z-\text{ideal}} + \underbrace{\frac{m}{n_{t}e}(n_{p}\partial_{t}\langle u_{pz}\rangle - n_{e}\partial_{t}\langle u_{ez}\rangle)}_{z-\text{temporal}} + \underbrace{\frac{m}{n_{t}e}(n_{p}\langle v_{px}\rangle\partial_{x}\langle u_{pz}\rangle - n_{e}\langle v_{ex}\rangle\partial_{x}\langle u_{ez}\rangle + n_{p}\langle v_{py}\rangle\partial_{y}\langle u_{pz}\rangle - n_{e}\langle v_{ey}\rangle\partial_{y}\langle u_{ez}\rangle)}_{z-\text{convective}} + \underbrace{\frac{1}{n_{t}e}(\partial_{x}\mathcal{T}_{pxz} - \partial_{x}\mathcal{T}_{exz}) - \frac{m}{n_{t}e}(\partial_{x}(n_{p}\langle v_{px}\rangle\langle u_{pz}\rangle) - \partial_{x}(n_{e}\langle v_{ex}\rangle\langle u_{ez}\rangle))}_{xz-\text{total}} + \underbrace{\frac{1}{n_{t}e}(\partial_{y}\mathcal{T}_{pyz} - \partial_{y}\mathcal{T}_{eyz}) - \frac{m}{n_{t}e}(\partial_{y}(n_{p}\langle v_{py}\rangle\langle u_{pz}\rangle) - \partial_{y}(n_{e}\langle v_{ey}\rangle\langle u_{ez}\rangle))}_{yz-\text{total}} + \underbrace{\frac{1}{n_{t}e}(\partial_{y}\mathcal{T}_{pyz} - \partial_{y}\mathcal{T}_{eyz}) - \frac{m}{n_{t}e}(\partial_{y}(n_{p}\langle v_{py}\rangle\langle u_{pz}\rangle) - \partial_{y}(n_{e}\langle v_{ey}\rangle\langle u_{ez}\rangle))}_{yz-\text{thermal}}}_{yz-\text{thermal}}$$

$$(1)$$

hierarchical plasmoid chain (panel (A)), plasma is continuously advected into the central region (panel (B)) by the reconnection process and pushed out along the sheet. The nonideal electric field E_z^* is the nonvanishing electric field in the frame comoving with the mean particle velocity (i.e., the comoving frame). In magnetic X-points, where the magnetic field reconnects (i.e., changes topology), an out-of-plane nonideal electric field E_z^* (panel (C)) is created and magnetic energy is dissipated. Furthermore, an out-of-plane current density j_z (panel (D)) is created in the reconnection layer.

We investigate the reconnection process in nonideal reconnection regions (from here on: reconnection regions), defined as $|E_z| > (B_x^2 + B_y^2)^{1/2}$ (panel (E)), with E_z the total out-of-plane electric field, where for the current sheet of Figure 1, $E_z < 0$ is expected for X-points of the main current sheet and $E_z > 0$ in between merging plasmoids (Sironi 2022). Comparison of panels (C) and (E) shows that this criterion captures regions well in which the nonideal electric field is strong. Moreover, with a guide field, the nonideal regions are well captured by this definition. In reconnection regions such as those located in the main current sheet and between plasmoid

Here, $\langle \mathbf{v}_t \rangle = (n_p \langle \mathbf{v}_p \rangle + n_e \langle \mathbf{v}_e \rangle)/n_t$ is the mean total particle three-velocity, $\langle \mathbf{v}_p \rangle = \langle \mathbf{u}_p / \gamma_p \rangle$ and $\langle \mathbf{v}_e \rangle = \langle \mathbf{u}_e / \gamma_e \rangle$ are the mean positron and electron three-velocity, $n_t = n_p + n_e$ is the total number density, n_p and n_e are the positron and electron number density, $\langle \mathbf{u}_p \rangle$ and $\langle \mathbf{u}_e \rangle$ are the spatial part of the mean positron and electron four-velocity, e is the elementary electric charge, $\mathcal{T}_\alpha = \int (m_\alpha \mathbf{u}_\alpha \mathbf{u}_\alpha / \gamma_\alpha) f_\alpha d^3 \mathbf{u}$ is the spatial part of the symmetric per-species total energy-momentum density tensor, \mathbf{u}_α is the spatial part of the particle four-velocity, γ_α is the particle Lorentz factor, and f_α is the per-species particle distribution function.

For later reference, the terms in Equation (1) are labeled with names that correspond to their physical interpretations, and they are given colors for convenience. The left-hand side represents the total electric field E_z in the z-direction. The first term (labeled z-ideal) on the right-hand side is the ideal electric field, which vanishes in the comoving frame. The remaining terms make up the nonideal electric field. The second term (z-temporal) arises from temporal changes in the species mean particle momenta, the third term from convective changes of the species mean particle momenta (z-convective), the fourth

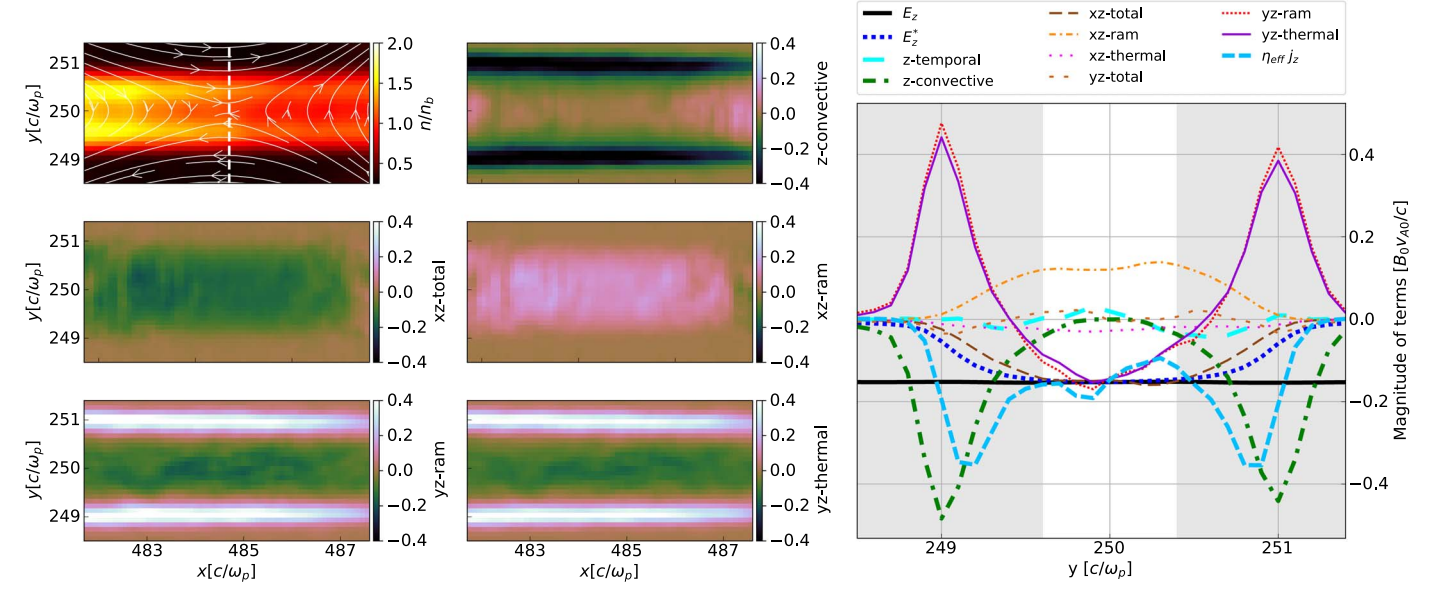


Figure 2. The spatial distributions of the density and relevant Ohm law terms in a typical X-point (indicated by the magnetic field lines as arrowed white lines in the top left panel) in the plasmoid chain without a guide field at $t = 0.5[L_x/c]$ in the six left and middle panels. In the right panel, (colored) profiles across the current sheet (along the dashed white line in the top left panel) with the reconnection region indicated by the nonshaded region. Near an X-point, the reconnection layer has a substructure that is formed by the individual profiles of contributions of Ohm's law terms. Inside the reconnection region, the reconnection electric field is primarily supplied by gradients of momentum fluxes. The electric field $\eta_{eff}j_z$ is an adequate approximation of the nonideal electric field E_z^* inside the reconnection region.

and sixth terms from the divergence of the total energy-momentum density tensor (xz-total and yz-total), and the fifth and seventh term from the divergence of the ram pressure tensor (xz-ram and yz-ram). The total energy-momentum density tensor and ram pressure tensor can be combined into a non-Lorentz-invariant and asymmetric tensor $P_{\alpha} = \mathcal{T}_{\alpha} - m_{\alpha}n_{\alpha}\langle v_{\alpha}\rangle\langle u_{\alpha}\rangle$, which is called throughout this work the thermal pressure tensor. This tensor shows some analogies to the thermal pressure tensor in the nonrelativistic case, but the actual thermal pressure tensor is only well defined in the comoving frame (a discussion of this tensor is given by Hesse & Zenitani 2007). The combination of the fourth with the fifth term and of the sixth with the seventh term then results in xz-thermal and yz-thermal, respectively, arising from the divergence of the thermal pressure tensor.

We first investigate the reconnection process in a single typical secondary X-point in the plasmoid chain before applying a statistical analysis to the full plasmoid chain. Figure 2 shows the spatial distributions of the density and relevant Ohm law terms (left and middle panels) around an X-point in the plasmoid chain without a guide field at $t=0.5[L_x/c]$ and $x=485[c/\omega_p]$. Additionally, it shows (colored) profiles (right panel) of Ohm law terms across the overdense current sheet (along the dashed white line in the top panel in the left column) through the X-point (indicated by the magnetic field lines as arrowed white lines). The reconnection region (i.e., $|E_z| > (B_x^2 + B_y^2)^{1/2}$) is indicated as the nonshaded region. All Ohm law terms in Figure 2 are in units of B_0v_{A0}/c .

In the upstream, as expected, all nonideal terms, i.e., the nonideal electric field E_z^* vanish (blue line in the right panel). Particles move from upstream regions toward the current sheet from both sides, carrying mainly y-momentum. The z-temporal term (cyan line in the right panel) has relatively small fluctuations around zero in the entire region.

Inside the reconnection region, $\langle v_{\alpha z} \rangle$ peaks, while $\langle v_{\alpha y} \rangle$ decreases and changes sign at the center, where the plasma flow

stagnates, coming from both sides. Furthermore, $\langle v_{\alpha z} \rangle$ only shows small variations along x. This leads to $n_{\alpha} \langle v_{\alpha y} \rangle \partial_y \langle u_{\alpha z} \rangle$ being the dominant term among the z-convective terms (top panel in the middle column and green line in the right panel) with peaks just outside, while it vanishes inside the reconnection region.

Next, we consider terms originating from the divergence of pressure tensors that include gradients of momentum fluxes (i.e., gradients of shear stresses). Throughout this work, we indicate momentum fluxes, being the transfer of the *k*th component of linear momentum into the *l*-direction, as *kl*-momentum flux. Considering the dynamics around an X-point described above, the ram *yz*-momentum flux peaks outside and decreases inside the reconnection region, where it changes sign at the center. This means that *yz*-ram (i.e., the *y*-gradient of ram *yz*-momentum flux; bottom panel in the left column and red line in the right panel) peaks just outside, and with opposite sign, it peaks again inside the reconnection region.

Particles from the upstream pass the magnetic field separatrices and are pushed downstream away from the X-point on both sides along the current sheet out of the reconnection region. This leads to an increase in their x-momentum and, therefore, their xz-momentum flux, which changes sign on the two sides of the X-point, while further downstream, it decreases as particles are no longer accelerated along x and z. This means that xz-ram (i.e., the x-gradient of xz-momentum flux; middle panel in the middle column and orange line in the right panel) peaks inside the reconnection region.

The total energy-momentum density tensor encompasses the ram pressure tensor, consisting of mean species velocities, and the thermal pressure tensor, consisting of thermal particle motion. When considering the gradients of momentum fluxes, it becomes immediately evident from the previous analysis together with Ohm's law (1) that only the gradients of thermal momentum fluxes matter for supplying the reconnection electric field, regardless of how its total pressure and ram pressure analogs contribute individually. Here, *xz*-thermal is

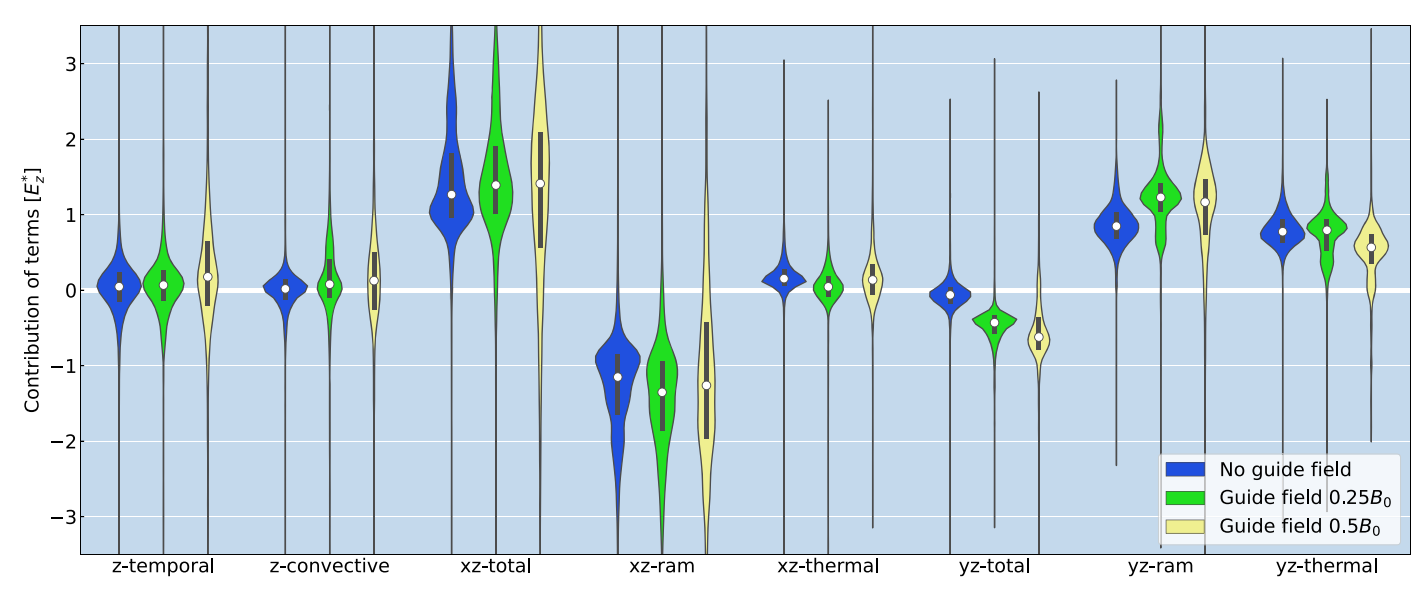


Figure 3. Violin plots showing the KDEs of the distributions of Ohm's law terms in all reconnection regions for the entire statistical steady state grouped by guide field strength for each term. Locally (in each cell of the reconnection region), each term is normalized to the local nonideal electric field such that the KDEs (colored regions) show the relative contribution of the terms to the local reconnection electric field. The thick black bars indicate interquartile ranges (i.e., the middle 50% of data points), and white dots indicate the medians.

negligibly small (magenta line in the right panel) with xz-total (middle panel in the left column and dark brown line in the right panel) and xz-ram having similar profiles, but of opposite sign. Furthermore, yz-thermal (bottom panel in the middle column and dark purple line in the right panel) is similar to yz-ram because yz-total (light brown line in the right panel) vanishes outside and is small inside the reconnection region.

This analysis shows that near the X-point, the contributions of individual Ohm law terms to the electric field have spatial distributions forming a substructure within the reconnection layer. While just outside the reconnection region, several terms contribute significantly to the electric field, inside the reconnection region, only the gradients of momentum fluxes contribute to the reconnection electric field. Furthermore, it shows that the reconnection region captures the inner region of the substructure well that is extremely localized around the X-point, where reconnection occurs, and it excludes the outer regions of the reconnection layer away from the X-point, thereby justifying our choice of the definition of the reconnection region. Moreover, this analysis indicates that in the reconnection region without a guide field, yz-thermal is the dominant term that drives the reconnection electric field.

3.2. Reconnection in the Full Plasmoid Chain without a Guide Field

In a fully developed self-similar hierarchical plasmoid chain, many different X-points exist that vary in their locations (e.g., in the main current sheet between plasmoids and in the current sheets between merging plasmoids), sizes, and (relativistic) velocities. In order to identify the reconnection mechanisms providing the reconnection electric field in all X-points of the full plasmoid chain, we use a statistical approach. We determine the contributions of Ohm's law terms to the reconnection electric field in the entire reconnection region of all X-points simultaneously during the entire statistical steady state.

Violin plots in Figure 3 show the distributions of Ohm's law terms grouped by guide field strength for each term. Herein, the

distributions are shown by kernel density estimations (KDEs) that are rotated on their side, such that the distributions run over the vertical axis, showing their median and spread. Moreover, the KDEs are mirrored along the vertical center line of each "violin", on which thick black bars indicate interquartile ranges (i.e., the middle 50% of data points, which is a measure for the spread), and white dots indicate the medians. In each cell of the reconnection regions, each contribution of the Ohm law terms is normalized to the local nonideal electric field such that these KDEs represent the relative contribution to the reconnection electric field.

When there is no guide field (left KDEs in blue in each grouped term in Figure 3), the distributions of *z*-temporal and *z*-convective are centered around zero, with a relatively small spread. Therefore, in a statistical sense, the contributions of these terms to the reconnection electric field vanish, which is expected based on the arguments presented in the previous analysis of a single X-point.

The distribution of *xz*-thermal is centered near zero, with a small spread making it statistically negligible, with distributions of *xz*-total and *xz*-ram that are similarly shaped, but opposite in sign. From Equation (1), this automatically means that only *yz*-thermal remains to supply the reconnection electric field. The distribution of *yz*-thermal is similar to *yz*-ram as the contribution of *yz*-total is statistically very small.

The contributions of Ohm's law terms obtained in this statistical analysis of all X-points is in agreement with those obtained in the previous analysis of a single X-point. We therefore show for collisionless reconnection in the plasmoid-dominated regime without a guide field that yz-thermal is the dominant term that drives the reconnection electric field. Moreover, without a guide field, it is justified to approximate this driving term by its ram pressure analog (because yz-total is negligible), similar to Bessho & Bhattacharjee (2007), but now shown for all secondary X-points in a fully developed plasmoid chain.

This allows us to establish a useful expression for the effective resistivity. By first reducing the full Ohm law by neglecting all terms except yz-ram and then using the product rule, the

remaining terms are expanded into three subterms for each species α to $\partial_y(n_\alpha)\langle v_{\alpha y}\rangle\langle u_{\alpha z}\rangle + n_\alpha\partial_y(\langle v_{\alpha y}\rangle)\langle u_{\alpha z}\rangle + n_\alpha\langle v_{\alpha y}\rangle\partial_y(\langle u_{\alpha z}\rangle)$. From the previous analysis of a single X-point, we conclude that inside the reconnection region, $\langle v_{\alpha y}\rangle$ vanishes at the stagnation point, such that $\langle v_{\alpha y}\rangle \ll \langle u_{\alpha z}\rangle$ and $\partial_y\langle u_{\alpha z}\rangle \ll \partial_y\langle v_{\alpha y}\rangle$. This leads to $n_\alpha\partial_y(\langle v_{\alpha y}\rangle)\langle u_{\alpha z}\rangle$ being the dominant subterm, which is verified by our simulations. By simplifying Ohm's law (1) to the form $E_z^*=\eta_{\rm eff}j_z$, the ultimate effects of collisionless reconnection are gathered into an effective resistivity. Assuming charge neutrality $n_p=n_e$, from symmetry $-\langle u_{pz}\rangle=\langle u_{ez}\rangle$ and $\langle v_{py}\rangle=\langle v_{ey}\rangle=\langle v_y\rangle$ (all also shown from our simulations), and writing the dominant subterm in the form $\eta_{\rm eff}j_z$, with $j_z=-n_te\langle v_{\alpha z}\rangle$, an expression for the effective resistivity in a pair plasma without guide field is given by

$$\eta_{\text{eff}} = \frac{m}{n_t e^2} \frac{\langle u_{\alpha z} \rangle}{\langle v_{\alpha z} \rangle} \frac{\partial \langle v_y \rangle}{\partial y},\tag{2}$$

where α is one of either species. The expression is similar to Bessho & Bhattacharjee (2012), but now also shown to be valid for all reconnection regions in a fully developed plasmoid chain. The electric field $\eta_{\rm eff} j_z$ (dashed light blue line in the right panel of Figure 2), constructed from multiplying this expression (2) for the effective resistivity back with the out-of-plane current, is an adequate approximation to the nonideal electric field E_z^* (dotted blue line in the right panel of Figure 2) inside the reconnection region, especially at the center line of the current sheet (i.e., the X-point). Toward the boundary of the reconnection region (i.e., the intersection of the shaded and nonshaded region in the right panel of Figure 2), yz-thermal starts to deviate from E_7^* as other Ohm law terms (e.g., zconvective) become slightly nonzero. Furthermore, here $\eta_{\text{eff}}j_z$ slightly deviates from yz-thermal because the neglected terms in the expansion of yz-ram become slightly nonzero. Outside the reconnection region, the approximation of yz-thermal to E_z^* breaks down, and $\eta_{\text{eff}}j_z$ peaks due to stagnation of the inflow velocity through $\partial_{\nu}\langle \nu_{\nu}\rangle$.

Particles flowing from the upstream toward the X-point are accelerated by the reconnection electric field in the z-direction, after which the outflows diverge sideways. After a finite residence time τ in the accelerating reconnection region, particles are expelled into the downstream. The effective collisionless resistivity $\eta_{\rm eff} = m \langle \gamma_{\alpha z} \rangle / (n_t e^2 \tau)$ emerges from this finite residence time of the particles in the reconnection region such that $\tau = |\partial_y \langle v_{\alpha y} \rangle|^{-1} \sim d/v_{\rm in}$, with d the half-width of the current sheet, and $v_{\rm in}$ the inflow speed into the current sheet (Bessho & Bhattacharjee 2007). This is consistent with the classical collisionless inertial resistivity described by Speiser (1970).

3.3. Reconnection in the Full Plasmoid Chain with a Guide Field

Threading the system with a guide field affects the reconnection process and has been shown to slow it down. Hesse et al. (2004) find that in collisionless reconnection in the presence of moderate guide fields, two length scales are associated with the substructure of the reconnection layer. On

the scale of the electron skin depth, the convective contribution becomes equal to the ideal contribution. On the scale of the electron gyroradius (measured with respect to the guide field component), the thermal pressure-based contribution becomes equal to the convective contribution. This means that stronger guide fields lead to thinner reconnection regions (i.e., the inner substructure of the reconnection layer on the scale of the gyroradius), requiring higher numerical resolutions to be resolved, hence our choice for guide fields of moderate strength.

Although for the cases with a guide field (middle green and right yellow KDEs in each grouped term in Figure 3) the ztemporal and z-convective distributions show some changes in their shape and spread, statistically, their contributions remain nearly unaffected by the guide field and are negligible. In contrast to the findings of Hesse & Zenitani (2007), our statistical results of the entire plasmoid chain do not show a significant contribution of the z-temporal term. However, we are not in the same parameter regime because we employ more moderate guide fields (in contrast to their guide field strength of $1.5B_0$) and initialize particles with a lower temperature. Furthermore, their X-point is not part of a fully developed plasmoid chain in which secondary X-points form independently of the initial conditions. Moreover, the X-point may be going through a transient phase, which can potentially make them sensitive to the time-dependent term in Ohm's law. The xz-thermal contribution remains statistically negligible as distributions of xz-total and xz-ram show some changes, but remain similarly shaped and opposite in sign. The terms considered until now thus effectively remain unaffected by the guide fields and vanish, which automatically means that the only remaining term that matters for supplying the reconnection electric field regardless of the guide field strength is vzthermal, as shown in Figure 3. However, we find that a guide field does have a significant effect on the contributions of yztotal and yz-ram. With increasing guide field strength, the distribution of yz-total departs significantly from zero while retaining its relatively narrow spread. Moreover, the distribution of yz-ram shifts to become (in a statistical sense) larger than the reconnection electric field (i.e., centered around a value higher than 1 in Figure 3).

Here we have shown that relativistic collisionless plasmoidmediated reconnection (up to a guide field of $0.5B_0$) is predominantly driven by thermal pressure tensor gradients; more precisely, in a coordinate-independent description by the gradient, perpendicular to the current sheet, of flux, into the direction of the main current, of thermal momentum, perpendicular to the current sheet. Furthermore, the fact that in the presence of a guide field, yz-total departs statistically significantly from zero automatically means that yz-thermal cannot be approximated very well by yz-ram. Therefore, the expression for the effective resistivity with fluid-like quantities, initially proposed by Bessho & Bhattacharjee (2012) for a single X-point and shown above in Equation (2) to be valid for a full plasmoid chain of zero guide field, is no longer valid in the case with a guide field. In order to obtain an expression with single-fluid-like quantities available in an MHD description for the case with a guide field, it would be required to model the nongyrotropic thermal pressure component $P_{\alpha yz}$, which is beyond the scope of this work (Hesse et al. 2004; Most et al. 2022).

⁹ This Ohm law is actually only well defined in the comoving frame, but we determined that for our case, with only mildly relativistic bulk velocities in the reconnection regions, the differences arising from defining Ohm's law in the simulation domain frame versus the comoving frame are negligible.

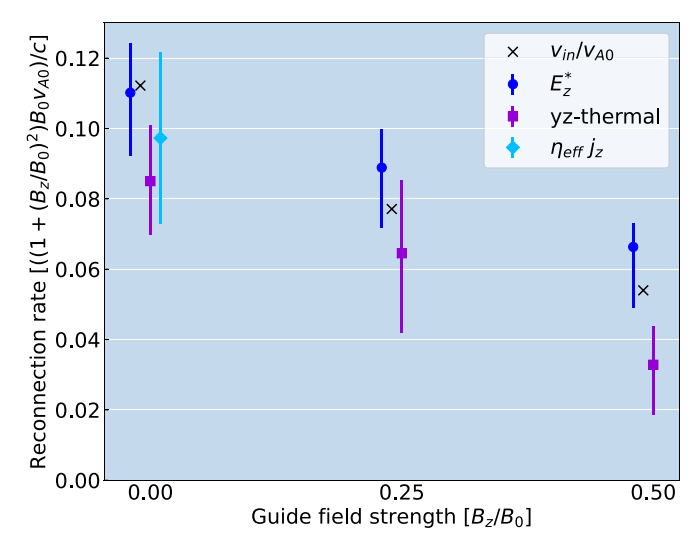


Figure 4. The medians and interquartile ranges of the distributions in units of $((1 + (B_z/B_0)^2)B_0\nu_{A0})/c$ of E_z^* (blue) and yz-thermal (dark purple) for all three guide field strengths and of $\eta_{\rm eff}j_z$ (light blue) for no guide field. Stronger guide fields lead to weaker reconnection electric fields. The dominant term yz-thermal decreases with the reconnection electric field. The measured inflow velocities (black crosses) due to an $E \times B$ -drift are in close agreement with the reconnection electric fields E_z^* , which directly corresponds to the reconnection rate.

In Figure 4, the medians (colored dots, squares, and diamond) and interquartile ranges (colored vertical bars) of the distributions of E_z^* (blue and dots) and yz-thermal (dark purple and squares) are shown for the three guide field strengths, and $\eta_{eff}j_z$ (light blue and diamond) is shown only for no guide field. These quantities are in units of $((1 + (B_z/B_0)^2)B_0v_{A0})/c$, comparable to a normalized reconnection rate. For no guide field, the electric field $\eta_{\text{eff}}j_z$ confirms our conclusion that the reduced yz-thermal term from Ohm's law, resulting in the expression (Equation (2)) for the effective resistivity, adequately approximates the reconnection electric field. This figure shows that a stronger guide field weakens the reconnection electric field. Up to a guide field strength of $0.25B_0$, the dominant term yz-thermal adequately approximates the reconnection electric field (i.e., reconnection rate), while for a guide field of $0.5B_0$, the deviation is larger. The reconnection rate obtained from the reconnection electric field is in agreement with the actual measured inflow velocity (black crosses).

4. Discussion and Conclusions

In this work, we identified the mechanisms driving the reconnection electric field for relativistic plasmoid-mediated reconnection in a collisionless pair plasma using a full Ohm law by means of a statistical analysis based on our 2D fully kinetic PIC simulations.

There are, however, certain limitations to our study. Although reconnection studies in 2D can capture many reconnection properties such as magnetic energy dissipation and particle acceleration, as shown in PIC simulations (Sironi & Spitkovsky 2014; Sironi 2022), in reality, reconnection occurs in 3D, where plasma turbulence may play a (dominant) role in the dissipation process and may affect a resistivity model. The plasma magnetization in neutron star or black hole magnetospheres is typically in the highly relativistic regime $(\sigma \gg 1)$, in accretion disks in the trans-relativistic regime

 $(\sigma \lesssim 1)$, and in black hole jet sheaths (Nathanail et al. 2020; Ripperda et al. 2020; Chashkina et al. 2021), it can be asymmetric ($\sigma \gg 1$ on one side, and $\sigma \lesssim 1$ on the other side). Asymmetric relativistic reconnection with different upstream properties on either side can result in different reconnection properties that are set by the upstream region with the lowest magnetization (Mbarek et al. 2022). For the highly relativistic regime, MHD simulations cannot achieve realistic plasma magnetizations due to density floors, whereas a force-free regime (i.e., the limit of infinite magnetization) is not suitable to describe reconnection and magnetic dissipation. PIC simulations, while capturing all the kinetic physics, cannot achieve a realistic scale separation between the astrophysical system size and skin depth. We conduct our reconnection analysis for $\sigma = 10$, giving a hierarchy of scales expected for the highly magnetized case such that the gyroradius is smaller than the electron skin depth, which in turn is smaller than the global scales of, for example, the length of macroscopic current sheets. In order to understand the resistivity model for reconnection in all these regimes, it would be useful to study a range of magnetizations, from the nonrelativistic limit to the near-force-free limit. Our study focused on pair plasmas, whereas in many astrophysical applications, ions may be a significant component of the plasma composition, affecting the reconnection. However, electron-ion reconnection in the highly relativistic regime should behave similarly to electron-positron reconnection (Guo et al. 2016; Werner et al. 2018). In the radiative reconnection regime that may be applicable around neutron stars and black holes (Uzdensky 2016; Beloborodov 2017), the interplay between radiation and collisionless plasma can result in extensive pair production, which affects the reconnection properties (Hakobyan et al. 2019), and, therewith, potentially the resistivity model. In our analysis, we consider only X-points as the nonideal regions, while in general, other nonideal regions may exist. However, X-points are likely to be the regions with the strongest nonideal effects.

For the case without a guide field from the dominant driving mechanism, an effective resistivity expression is formulated that is spatially nonuniform and peaks around the X-points. From this, we are able to estimate realistic values for the resistivity in an astrophysical system such as for the flaring region at the jet base in M87* (see the Appendix). Based on Ripperda et al. (2022) and Hakobyan et al. (2022), we estimate using Equation (2), an effective local X-point resistivity $\eta_{\rm eff} \sim 2.7 \cdot 10^{-1} [{\rm s}]$ that is higher than the magnetospheric upstream Spitzer resistivity $\eta_{\rm up} \sim 1.2 \cdot 10^{-24} [{\rm s}]$ by a factor of $\eta_{\rm eff}/\eta_{\rm up} \sim 2.3 \cdot 10^{23}$, implying a nonuniform nature of the resistivity. This nonuniform nature of the effective resistivity may qualitatively capture the properties of collisionless reconnection in an MHD description.

To conclude, the fully correct approach for incorporating the effects of collisionless reconnection into fluid-type models would be to include the Ohm law terms self-consistently in a nonideal or even two-fluid MHD description (Most et al. 2022). The approach we suggest as a first step is to determine the Ohm law term contributions and model essential parts of these terms into an ad hoc effective resistivity that depends on local fluid quantities (e.g., Ripperda et al. 2019) in resistive relativistic MHD (Del Zanna et al. 2016; Ripperda et al. 2019). Based on the results of this work, we propose a nonuniform effective resistivity that is negligible on global scales and becomes significant only locally in X-points to mimic the properties of relativistic collisionless

reconnection in nonideal MHD simulations. This model can provide a viable opportunity to accurately model the reconnection properties powering high-energy emission and design physically grounded global models for it.

Acknowledgments

S.S. would like to thank Sasha Philippov, Hayk Hakobyan, and Amir Levinson for their help. B.R. would additionally like to thank Amitava Bhattacharjee, Sasha Chernoglazov, and Elias Most for useful discussions. Support for this work was provided by NASA through the NASA Hubble Fellowship grant No. HST-HF2-51518.001-A awarded by the Space Telescope Science Institute, which is operated by the Association of Universities for Research in Astronomy, Incorporated, under NASA contract No. NAS5-26555. F.B. acknowledges support from the FED-tWIN program (profile Prf-2020-004, project "ENERGY") issued by BELSPO. The use of the national computer facilities in this research was subsidized by NWO Domain Science under grant No. 2021.001. The computational resources and services used in this work were partially provided by facilities supported by the Scientific Computing Core at the Flatiron Institute, a division of the Simons Foundation; by the VSC (Flemish Supercomputer Center), funded by the Research Foundation Flanders (FWO) and the Flemish Government - department EWI. R.K. acknowledges funding from the European Research Council (ERC) under the European Union's Horizon 2020 research and innovation program (grant agreement No. 833251 PROMI-NENT ERC-ADG 2018), internal funds KU Leuven project C14/19/089 TRACESpace and the Research Foundation Flanders (FWO) project G0B4521N on flares. L.S. acknowledges support from the Cottrell Scholars Award, DoE DE-SC0021254 and NSF AST-2108201.

Appendix Estimation of Resistivities in the Flaring Region of M87*

Reconnection as a flare mechanism for active galactic nuclei (AGN) has been proposed by Broderick & Loeb (2006), Younsi & Wu (2015), Ball et al. (2016), Dexter et al. (2020), Porth et al. (2021), and Scepi et al. (2022) and was shown to occur in 2D by Nathanail et al. (2020), Ripperda et al. (2020), and Chashkina et al. (2021) and in 3D by Ripperda et al. (2022), and Nathanail et al. (2022). In the magnetically arrested disk model, the most energetic flares originate close to the event horizon (Ripperda et al. 2022) from reconnection sites, without a guide field, fed by highly magnetized pair plasma from the jet. As an example for AGN flares, we use the well-constrained conditions of M87* to illustrate the nonuniformity between the global upstream resistivity and the local effective X-point resistivity for the flaring region at the jet base.

During the flaring state, the synchrotron-produced photons from reconnection-accelerated particles in the current sheet produce secondary pairs through photon-photon collisions in the upstream. At the time of birth, these secondary pairs are estimated to have a characteristic Lorentz factor $\gamma_{\rm sec}\approx 200$ (Hakobyan et al. 2022) setting the characteristic temperature dictated by the synchrotron burnoff limit as $k_{\rm B}T/(mc^2)=\gamma_{\rm sec}/3\approx 200/3$. This gives an upstream Spitzer resistivity due to Coulomb collisions of pairs of $\eta_{\rm up}=(k_{\rm B}T/(mc^2))^{-3/2}4$ $\sqrt{2\pi}\,e^2\ln(\Lambda)/(3mc^3)\sim 1.2\cdot 10^{-24}[{\rm s}]$ with the Coulomb logarithm $\ln(\Lambda)=21$.

The fiducial parameters for M87* are an upstream magnetic field strength $B_{\rm up}=10^2[G]$ at the event horizon, a central mass $M=6\cdot 10^9[M_\odot]$, and a multiplicity $\tilde{\lambda}=10^8$ for the pair production during the flaring state (Ripperda et al. 2022). Using the Goldreich-Julian density leads to a particle density $n\sim 1.9\cdot 10^3(\tilde{\lambda}/10^8)(M/(6\cdot 10^9M_\odot))^{-1}(B_{\rm up}/10^2[{\rm G}])~[{\rm cm}^{-3}],$ giving a plasma skin depth $\lambda_p=c/\omega_{\rm p}=(m_ec^2/(4\pi ne^2))^{1/2}\sim 1.2\cdot 10^4(\tilde{\lambda}/10^8)^{-1/2}(M/(6\cdot 10^9M_\odot))^{1/2}(B_{\rm up}/10^2[{\rm G}])^{-1/2}[{\rm cm}]$ and an upstream plasma magnetization $\sigma_{\rm up}=B^2/(4\pi nmc^2)\sim 5.2\cdot 10^5~(\tilde{\lambda}/10^8)^{-1}(M/(6\cdot 10^9M_\odot))~(B_{\rm up}/10^2[{\rm G}])$ during the flaring state.

To estimate the X-point resistivity, we further inspect Equation (2), which can be recast into $\eta_{\rm eff}=4\pi/c^2\,\lambda_{\rm p}\langle\gamma_{\alpha z}\rangle\nu_{\rm in},$ where $\langle\gamma_{\alpha z}\rangle:=\langle u_{\alpha z}\rangle/\langle v_{\alpha z}\rangle$. The latter factor comes from the relativistically increased inertia of the accelerated particles in the X-points and is not present in the nonrelativistic treatment (see also Bessho & Bhattacharjee 2012). Here we have also used that the inflow velocity $\nu_{\rm in} \sim \langle v_{\alpha y}\rangle \sim 0.1c$ changes over the (half-)width of the current sheet on the scale of the skin depth, giving $\partial_y \langle v_{\alpha y}\rangle \sim \nu_{\rm in}/\lambda_p$. The upstream plasma magnetization sets the available magnetic energy per particle and thus $\langle\gamma_{\alpha z}\rangle\sim\sigma_{\rm up}$ (Sironi & Spitkovsky 2014), such that for the fiducial M87* parameters, we have $\eta_{\rm eff}\sim 4\pi\sigma_{\rm up}\lambda_p 0.1/c=2.7\cdot 10^{-1}[s]$, which is larger than the upstream resistivity by a factor of $\eta_{\rm eff}/\eta_{\rm up}\sim 2.3\cdot 10^{23}$.

ORCID iDs

S. Selvi https://orcid.org/0000-0001-9508-1234
O. Porth https://orcid.org/0000-0002-4584-2557
B. Ripperda https://orcid.org/0000-0002-7301-3908
F. Bacchini https://orcid.org/0000-0002-7526-8154
L. Sironi https://orcid.org/0000-0002-1227-2754

R. Keppens https://orcid.org/0000-0003-3544-2733

References

```
Ball, D., Özel, F., Psaltis, D., & kwan Chan, C. 2016, ApJ, 826, 77
Beloborodov, A. M. 2017, ApJ, 850, 141
Bessho, N., & Bhattacharjee, A. 2007, PhPl, 14, 056503
Bessho, N., & Bhattacharjee, A. 2012, ApJ, 750, 129
Bransgrove, A., Ripperda, B., & Philippov, A. 2021, PhRvL, 127, 055101
Broderick, A. E., & Loeb, A. 2006, MNRAS, 367, 905
Cerutti, B., Uzdensky, D. A., & Begelman, M. C. 2012, ApJ, 746, 148
Chashkina, A., Bromberg, O., & Levinson, A. 2021, MNRAS, 508, 1241
Comisso, L., & Bhattacharjee, A. 2016, JPlPh, 82, 595820601
Del Zanna, L., Papini, E., Landi, S., Bugli, M., & Bucciantini, N. 2016,
Dexter, J., Tchekhovskoy, A., & Jiménez-Rosales, A. 2020, MNRAS,
   497, 4999
Giannios, D. 2013, MNRAS, 431, 355
Guo, F., Li, X., Li, H., et al. 2016, ApJL, 818, L9
Hakobyan, H., Philippov, A., & Spitkovsky, A. 2019, ApJ, 877, 53
Hakobyan, H., Ripperda, B., & Philippov, A. 2023, ApJL, 943, L29
Hakobyan, H., & Spitkovsky, A. 2020, Multi-species particle-in-cell plasma
  code, GitHub, https://ntoles.github.io/tristan-wiki,
Hesse, M., Kuznetsova, M., & Birn, J. 2004, PhPl, 11, 5387
Hesse, M., & Zenitani, S. 2007, PhPl, 14, 112102
Hu, R., & Beloborodov, A. M. 2021, arXiv:2109.03935
Keppens, R., Porth, O., Galsgaard, K., et al. 2013, PhPl, 20, 092109
Lyubarsky, Y. 2018, MNRAS, 483, 1731
Lyubarsky, Y. 2020, ApJ, 897, 1
Lyubarsky, Y. E. 2012, MNRAS, 427, 1497
Lyutikov, M., & McKinney, J. C. 2011, PhRvD, 84, 084019
Lyutikov, M., & Popov, S. 2020, arXiv:2005.05093
Mahlmann, J. F., Philippov, A. A., Levinson, A., Spitkovsky, A., &
  Hakobyan, H. 2022, ApJL, 932, L20
Mbarek, R., Haggerty, C., Sironi, L., Shay, M., & Caprioli, D. 2022, PhRvL,
   128, 145101
```

```
Most, E. R., Noronha, J., & Philippov, A. A. 2022, MNRAS, 514, 4989
Most, E. R., & Philippov, A. A. 2020, ApJ, 893, L6
Most, E. R., & Philippov, A. A. 2022, arXiv:2207.14435
Nathanail, A., Fromm, C. M., Porth, O., et al. 2020, MNRAS, 495, 1549
Nathanail, A., Mpisketzis, V., Porth, O., Fromm, C. M., & Rezzolla, L. 2022, MNRAS, 513, 4267
Parfrey, K., Beloborodov, A. M., & Hui, L. 2012, ApJ, 754, L12
Petropoulou, M., Giannios, D., & Sironi, L. 2016, MNRAS, 462, 3325
Philippov, A., Uzdensky, D. A., Spitkovsky, A., & Cerutti, B. 2019, ApJ, 876, L6
Philippov, A. A., & Spitkovsky, A. 2018, ApJ, 855, 94
Porth, O., Mizuno, Y., Younsi, Z., & Fromm, C. M. 2021, MNRAS, 502, 2023
Ripperda, B., Bacchini, F., & Philippov, A. A. 2020, ApJ, 900, 100
```

Ripperda, B., Bacchini, F., Porth, O., et al. 2019, ApJS, 244, 10

Ripperda, B., Liska, M., Chatterjee, K., et al. 2022, ApJL, 924, L32

```
Ripperda, B., Porth, O., Sironi, L., & Keppens, R. 2019, MNRAS, 485, 299
Scepi, N., Dexter, J., & Begelman, M. C. 2022, MNRAS, 511, 3536
Sironi, L. 2022, PhRvL, 128, 145102
Sironi, L., & Beloborodov, A. M. 2020, ApJ, 899, 52
Sironi, L., & Spitkovsky, A. 2014, ApJ, 783, L21
Speiser, T. 1970, P&SS, 18, 613
Sridhar, N., Sironi, L., & Beloborodov, A. M. 2021, MNRAS, 507, 5625
Sridhar, N., Sironi, L., & Beloborodov, A. M. 2022, arXiv:2203.02856
Uzdensky, D. A. 2016, Magnetic Reconnection, Vol. 427 (Berlin: Springer), 473
Uzdensky, D. A., Loureiro, N. F., & Schekochihin, A. A. 2010, PhRvL, 105, 235002
Werner, G., Uzdensky, D., Begelman, M., Cerutti, B., & Nalewajko, K. 2018, MNRAS, 473, 4
```